nature synthesis

Article

https://doi.org/10.1038/s44160-024-00660-z

Metal/MXene composites via in situ reduction

Received: 22 August 2023

Accepted: 6 September 2024

Published online: 4 October 2024

Check for updates

Qingxiao Zhang[1,2,6], Jia-ao Wang[3,6], Qinghua Yu[2,6], Qizhen Li[4,6], Runze Fan[1], Chong Li[1], Yiyi Fan[2], Cong Zhao[2], Weihua Cheng[1], Peiyi Ji[1], Jie Sheng[1], Chenhao Zhang[1], Songhai Xie[5], Graeme Henkelman[3] & Hui Li[1]

Metal/two-dimensional substrate composites offer a rich library of materials that can have application in catalysis, sensing, biotechnology and other fields. In situ reduction deposition provides a scalable method for fabricating metal/MXene composites, but the rational control of metal nanostructures growth on MXene remains difficult. Here a strategy for the in situ reduction deposition of various metals (Au, Pd, Ag, Pt, Rh, Ru and Cu) on $Ti_3C_2T_x$ MXene is demonstrated. This study uncovers the guiding principles of the metal deposition process on MXene nanosheets, including the influence of redox potential, metal coordination and lattice mismatch. A series of metal/MXene composites with fine-tuned structures were constructed based on these guiding principles, such as Pd@$Au_{\text{-Edge}}$/$Ti_3C_2T_x$, Pt@$Au_{\text{-Edge}}$/$Ti_3C_2T_x$, Au@Ag@$Au_{\text{-Surface}}$/$Ti_3C_2T_x$ and Ag@Pd@$Au_{\text{-Edge}}$/$Ti_3C_2T_x$. In addition, the in situ reduction strategy can be extended to other MXene materials, such as Mo_2CT_x, V_2CT_x, Ti_3CNT_x, $Nb_4C_3T_x$ and $Mo_2TiC_2T_x$, which allows the creation of metal/MXene composites with versatile and customizable nanostructures for a wide range of applications.

Two-dimensional (2D) material-based noble metal heterostructures have interesting photonic[1,2], electronic[3,4] and catalytic properties[5–7]. In catalysis, for example, the ability to precisely tailor the size[8], location[9] and hybrid structures[10,11] of metals at the nano or atomic scale is becoming increasingly important as it allows a better understanding of the active sites of metals. However, precise control over metal nanostructures on 2D supports remains challenging due to the intricate interactions among supports, metal precursors, solvents, reducing agents and even surfactants[12,13].

MXene materials are regarded as ideal templates for synthesizing functional composites[14–20]. The presence of reducible substances on the surface of MXene materials provides an accessible chemical pathway for constructing heterostructures of metals and 2D materials[21–29]. This is achieved by reducing metal ions to low-valence monoatomic or metallic nanoparticles without the need for additional reducing agents. This is generally ascribed to the in situ reduction (self-reduction) strategy, where the transition metal in the metastable state of the 2D MXene acts as a reducing agent, facilitating the formation of a chemical bond between the MXene and the metal[21,27,30]. Using MXene materials as reductive carriers for monoatomic metal loading has been widely investigated[27,31]. However, understanding of the in situ reduction strategy remains limited, and precise control of metal growth on MXenes is still challenging[29,30,32]. A deeper comprehension of the nucleation and growth processes of metals on 2D MXenes is essential for the rational design of new composite systems.

In this Article, we investigate the deposition of Au, Pd, Ag, Pt, Rh, Ru and Cu on the $Ti_3C_2T_x$ surface through in situ reduction in an aqueous environment. Most metals, including Pt, Ru, Rh and Cu, initially adopt

[1]Key Laboratory of Resource Chemistry of Ministry of Education, Shanghai Key Laboratory of Rare Earth Functional Materials, and Department of Chemistry, Shanghai Normal University, Shanghai, China. [2]College of Chemistry and Chemical Engineering, Shandong University of Technology, Zibo, China. [3]Department of Chemistry and the Oden Institute for Computational Engineering and Sciences, The University of Texas at Austin, Austin, TX, USA. [4]School of Materials, University of Manchester, Manchester, UK. [5]Department of Chemistry and Shanghai Key Laboratory of Molecular Catalysis and Innovative Materials, Fudan University, Shanghai, China. [6]These authors contributed equally: Qingxiao Zhang, Jia-ao Wang, Qinghua Yu, Qizhen Li. e-mail: lihui@shnu.edu.cn

https://doi.org/10.1038/s44160-024-00660-z

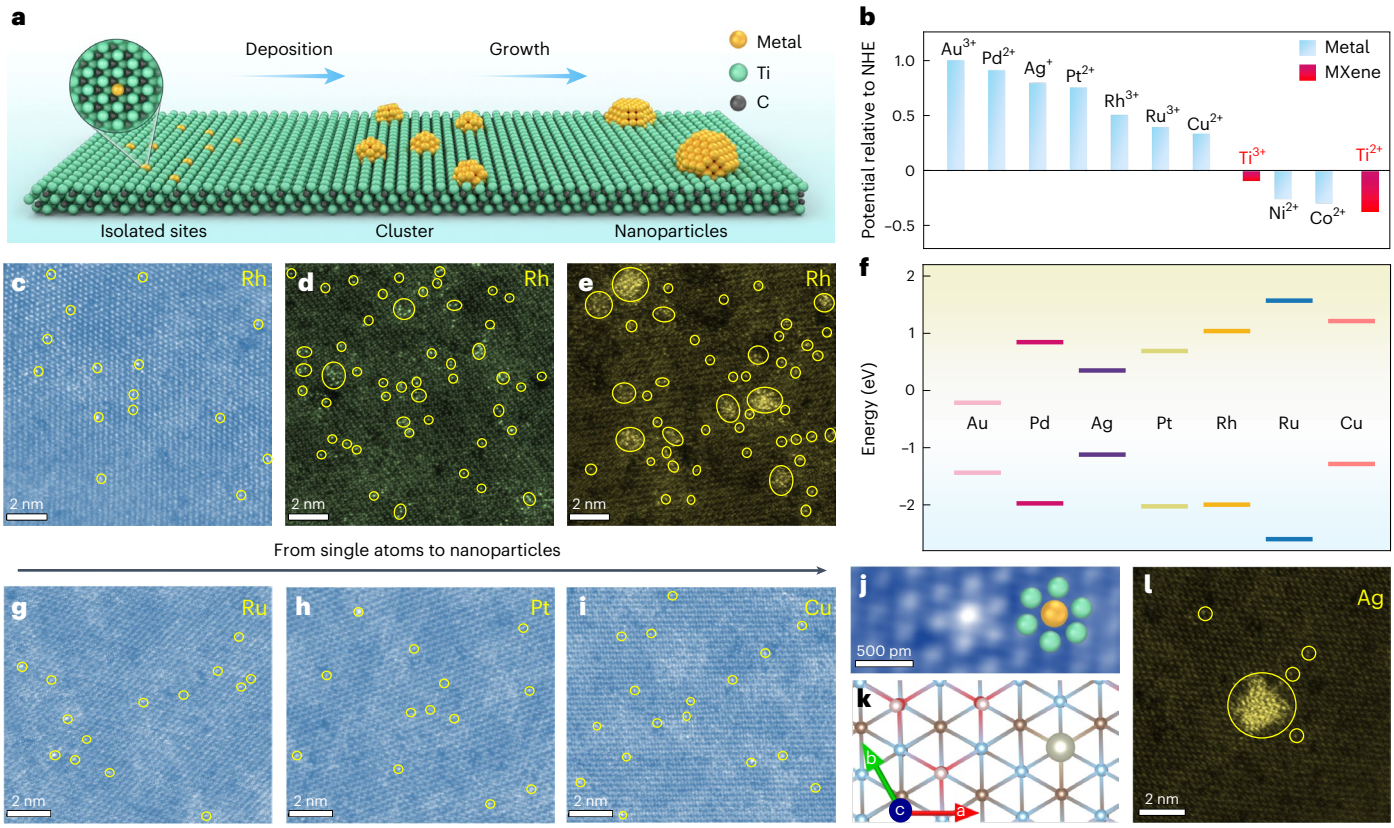

Fig. 1 | A preliminary exploration of in situ reduction processes—nucleation and growth. a, A schematic illustration of metal depositing on the surface of MXene by in situ reduction. **b**, A comparison of redox potentials of the $Ti_3C_2T_x$ MXene and metal ions. **c**–**e**, HAADF–STEM images of Rh/$Ti_3C_2T_x$ with Rh loadings of 0.2 wt% (**c**), 0.5 wt% (**d**) and 2 wt% (**e**). **f**, Adsorption energies of different metal ions on $Ti_3C_2T_x$ nanosheets with and without vacancies showing that the adsorption energy at the vacancy is lower. **g**–**i**, HAADF–STEM images of Ru/$Ti_3C_2T_x$ (**g**), Pt/$Ti_3C_2T_x$ (**h**) and Cu/$Ti_3C_2T_x$ (**i**) with 0.2 wt% loadings. **j**, A magnified HAADF–STEM image of Rh/$Ti_3C_2T_x$ with an inset showing the simulated distribution of Rh and Ti atoms on the Rh/$Ti_3C_2T_x$ surface. The simulated image is in good agreement with the experimental results. **k**, The top view of the slab models used to describe the Rh/$Ti_3C_2T_x$ MXene. The atoms in blue, grey, brown and red represent Ti, Rh, C and O, respectively. **l**, HAADF–STEM image of Ag/$Ti_3C_2T_x$ with 0.2 wt% loading. The vectors a, b and c represent a non-orthogonal coordinate system in **k**. The angle between a and b is 120° and c is aligned parallel to the direction of the cross product of a and b.

a monoatomic state at extremely low loadings and transition to a nanoparticle state with increasing loading. Au, Ag and Pd nanoparticles have markedly different distributions, ranging from a worm-like structure of Pd at various loadings to an uneven deposition of Ag. The growth mechanism of these metals can be applied to other MXene substrates, such as Mo_2CT_x, V_2CT_x, Ti_3CNT_x, $Nb_4C_3T_x$ and $Mo_2Ti_2C_3T_x$. Interestingly, Au nanoparticles are uniformly deposited at the edges of the $Ti_3C_2T_x$ MXene, a feature that can be tuned by modifying the coordination environment. Further investigation uncovers the important role of redox potential, metal coordination and lattice mismatch in guiding the metal deposition process on MXene nanosheets. An awareness of these deposition behaviours aids the design and synthesis of MXene noble metal heterostructures with precise structures, achieved by controlling the deposition sequences. Furthermore, the regulation of metal size, deposition location and structure can be realized through an in situ reduction strategy. Since reductive metal species are ubiquitous in all MXenes, this strategy is likely to pave the way for the precise design of metal/MXene composites with defined target structures.

Results and discussion

The $Ti_3C_2T_x$ MXene prepared by liquid exfoliation[33–35] served as an ideal support for the study of the in situ reduction strategy exhibiting typical 2D structures and abundant reduction sites on its surface (Fig. 1a and Supplementary Figs. 1–9). To carry out the liquid-phase metal deposition, the $Ti_3C_2T_x$ MXene acted as both a carrier and a reducing agent[27], while water served as a cleaning solvent in this process. This resulted in the formation of hybrid materials termed M/$Ti_3C_2T_x$, where M represents metals in their reduced state.

Preliminary investigation of in situ reduction deposition

To ascertain the valence states of the reduced metals, X-ray photoelectron spectroscopy (XPS) spectra were obtained from powder samples after centrifugation, washing and drying. As shown in Supplementary Fig. 10, Ag^+, Au^{3+}, Pd^{2+}, Pt^{2+}, Rh^{3+}, Ru^{3+} and Cu^{2+} are reduced, while the valence states of Ni^{2+} and Co^{2+} remain unchanged. It is important to note that the solvent (water) and the experimental conditions (absence of any additional reducing agent or strong light irradiation) are incapable of reducing M^{n+} ions, suggesting that the $Ti_3C_2T_x$ nanosheets play a key role in the reduction process.

To elucidate the reduction mechanism, it is first necessary to identify the reducing species on the surface of $Ti_3C_2T_x$ MXene. Potential sources include surface Ti species[30,36], Ti vacancies[26] and surface groups[29,37]. XPS spectra of $Ti_3C_2T_x$ MXene (Supplementary Fig. 9) confirm that Ti species in the nanosheets are mainly present in low-valence forms, with peaks at 455.8 and 457.1 eV corresponding to the $2p_{3/2}$ spectra of Ti^{2+} and Ti^{3+}, respectively[38,39]. Both Ti species have lower redox potentials compared with Cu^{2+} (+0.34 V versus normal hydrogen electrode (NHE) for Cu^{2+} and −0.37 V versus NHE for Ti^{2+}) and even have the potential to reduce Co^{2+} and Ni^{2+} (Fig. 1b and Supplementary Table 1). XPS analysis of M/$Ti_3C_2T_x$ also shows an increase in the Ti^{4+} fraction, rising from 6.9% to 16.9% after metal deposition (Supplementary Figs. 9 and 11). Therefore, it can be concluded that the redox reaction between

the low-valence Ti species (Ti^{2+}/Ti^{3+}) and the metal is the driving force of the in situ reduction process. During the in situ reduction deposition process, the metal exhibits a characteristic nucleation growth pattern. Taking Rh^{3+} as an example, it initially disperses in the form of single atoms at low loading concentrations and as the loading increases, metal clusters and small metal nanoparticles gradually form (Fig. 1c–e).

The nucleation site of the metal is crucial for the formation of $M/Ti_3C_2T_x$ composites. Inevitably, Ti vacancies appear on the surface of the MXene material as a result of liquid-phase etching[40] (Supplementary Fig. 6). Density functional calculations were performed on $Ti_3C_2T_x$ nanosheets with and without Ti vacancies to investigate how $Ti_3C_2T_x$ MXene can act as an electron donor for M^{n+} reduction (Supplementary Figs. 12–15). Figure 1f shows that single metal atoms anchored to vacancies have lower free energy. Therefore, single atoms tend to be deposited at the Ti vacancies of $Ti_3C_2T_x$ MXene (Supplementary Table 2). The high-angle annular dark-field scanning transmission electron microscopy (HAADF–STEM) images (Fig. 1g,h) reveal that Ru, Pt and Cu can exist as single atoms at low loading. Furthermore, the HAADF–STEM image confirms that single Rh atoms are anchored to Ti vacancies, which is attributed to the larger atomic number of Rh, resulting in a higher contrast compared with Ti atoms. These results are in agreement with our calculations (Fig. 1j,k). Extended X-ray absorption fine structure (EXAFS) spectra also show that at a low loading of 0.2 wt% (W_{metal}/W_{MXene}), the metals Rh, Ru, Pt and Cu all exhibit single-atom characteristics (Supplementary Figs. 16–19 and Supplementary Tables 3–6). The single-atom dispersion state at low loading has been extensively reported and analysed in the literature[27,28,41]. This dispersion state is strongly dependent on the concentration of atomic-level vacancies on the surface of the $Ti_3C_2T_x$ nanosheets. It is crucial to effectively regulate these vacancies as they serve as preferred sites for spontaneous reduction, nucleation and subsequent growth of M^{n+}.

The reduction of noble metals and Cu^{2+} was further verified by liquid-phase reduction experiments. In the X-ray absorption near-edge structure spectra, the absorption edge of $Cu/Ti_3C_2T_x$ lies between that of Cu foil and CuO, indicating that the individual Cu oxidation states range between 0 and +2 (Supplementary Fig. 20). Further analysis of the XPS spectra of $M/Ti_3C_2T_x$ reveals a higher proportion of Ti^{4+} compared with freshly prepared $Ti_3C_2T_x$ MXene (Supplementary Fig. 11), consistent with oxidation of $Ti_3C_2T_x$. Accordingly, the reduction of M^{n+} species can be attributed to the donation of electrons from Ti^{2+} and Ti^{3+} during the oxidation of MXene[27].

Further investigation is required to understand the changes in metal deposition behaviour with increasing loading. The deposition of Ag^{+} is taken as an example. Ag has a high redox potential and should be highly susceptible to redox reactions with electron donors (that is, Ti^{2+} and Ti^{3+} in $Ti_3C_2T_x$ MXene). However, a low loading of Ag (0.2 wt%) deposited on the MXene surface results in the coexistence of single atoms and metal nanoparticles (Fig. 1l and Supplementary Fig. 21). Although achieving entirely single-atomic sites at low loadings is feasible, this approach has limited practical value, particularly in single-atom catalysis, and falls outside the scope of precise spectroscopy characterization[42]. As the loading is increased (as shown in Supplementary Figs. 22–24), the Ag nanoparticles grow in size without adopting a fixed morphology, forming nanoparticles piles. This indicates that Ag follows a nucleation growth pattern during in situ reduction deposition on the MXene surface.

Leaching of Ti during metal deposition

We investigate the impact of the amount of metal deposited by in situ reduction on the composites structure. During the in situ reduction process, an exsolution of Ti was observed from the $Ti_3C_2T_x$ support (Fig. 2a,b and Supplementary Fig. 25). HAADF–STEM images also show that the deposition of metal subsets including Rh, Ru and Pt leads to substantial defect formation (Supplementary Figs. 26–28). In contrast, there is minimal loss of Ti element from the aqueous $Ti_3C_2T_x$ MXene solutions in a resting state[43]. The solid precipitate obtained from the filtered liquid after freeze drying is primarily composed of $TiCl_{3.59}F_{3.03}C_{0.58}O_x$, where the element Ti is in the +4 valence state by XPS results (Fig. 2c). Furthermore, the results of EXAFS show that the coordination structures of Ti in precipitate were mainly Ti-F, Ti-Cl or Ti-O, whereas the Ti species in $Au_W/Ti_3C_2T_x$ did not undergo notable changes in their Ti coordination environment after the Au loading, which indicated that leached Ti^{4+} did not produce TiO_2 preferentially in solution or on MXene substrate (Supplementary Figs. 29–34 and Supplementary Table 7). The presence of Ti in an oxidized state may have been overlooked previously due to different methods of sample preparation. The loss of transition metal elements (for example, Ti in $Ti_3C_2T_x$ MXene) could possibly explain why MXenes fail to retain their 2D structure after oxidation[44,45].

To further clarify the spatio-temporal sequence between redox reactions and element loss, we conducted control experiments based on the primary cell reaction mechanism (Fig. 2e,f and Supplementary Figs. 35–37). In this case, the reduction of Au^{3+} can occur regardless of whether M^{n+} is in direct contact with MXene or not, without the need for other reducing substances in the solution (please note that the pathway for redox electron transfer is essential). Here, two different environments for $Ti_3C_2T_x$ have been created using the graphite crucible and dialysis membranes (cut-off molecular weight of 5,000), where the dialysis membranes allow the elemental Ti to escape. The XPS spectra show a considerable increase in the Ti^{4+} fraction of $Ti_3C_2T_x$ located in the graphite crucible (13.7%), while it remains at a low level (4.7%) when $Ti_3C_2T_x$ is located in the dialysis membrane (Fig. 2e,f). From these observations, we can deduce that (1) the redox reaction between $Ti^{2+/3+}$ and M^{n+} is an inherently in situ reduction, (2) the redox reaction can occur through charge transfer without requiring direct contact between the two components and (3) Ti^{4+} generated by oxidation tends to leach into solution. These findings also explain the deposition of metal nanoparticles on the surface of $Ti_3C_2T_x$ MXene rather than the formation of a homogeneous metal layer on the surface. The viability of metal reduction is dictated by the redox potential between MXenes and metal ions, along with the electron transfer. Concurrently, the environment of MXene deposition site is the pivotal factor in determining the deposition rate, the deposition location and the morphology of the deposited metal.

Selectivity of Au deposition location

In addition to controlling the amount and size of deposited metal, we have successfully obtained $Au/Ti_3C_2T_x$ samples with controllable deposition locations through in situ reduction deposition. When $Ti_3C_2T_x$ aqueous dispersion is used as a reducing agent, Au nanoparticles with low loading selectively grow at the edges of the MXene material, resulting in a distribution of Au nanoparticles with a size of 7 ± 4 nm at 2 wt% loading (Fig. 3a–c). Even during the in situ reduction deposition of highly loaded Au, linearly arranged Au nanoparticles can still be observed, indicating that the selective deposition of Au at edge sites is not a random occurrence (Supplementary Fig. 38). Instead, it follows an edge-first surface pattern, with deposition on the surface only occurring when the edge sites are saturated. The edge-loaded Au nanoparticles exhibit a morphology similar to that of Au nanodecahedrons[46] (Fig. 3d,e) and HAADF–STEM images reveal inter stripe distances of 0.241 nm and 0.210 nm, corresponding to the lattice spacings of the Au (111) and Au (200) planes, respectively. This unique edge deposition mode and the structure of the Au nanocrystals provide additional possibilities for the in situ reduction deposition of metals on the surface of $Ti_3C_2T_x$ nanosheets.

Selective deposition at edge sites using Au nanodecahedrons provides insights into in situ reduction processes (for example, competing reduction reactions; Supplementary Fig. 39), which are crucial for assessing the electron-donating capability of thin-layered $Ti_3C_2T_x$ nanostructures at room temperature. The preferential deposition of Au nanoparticles at the edge of MXene material is directly related to

https://doi.org/10.1038/s44160-024-00660-z

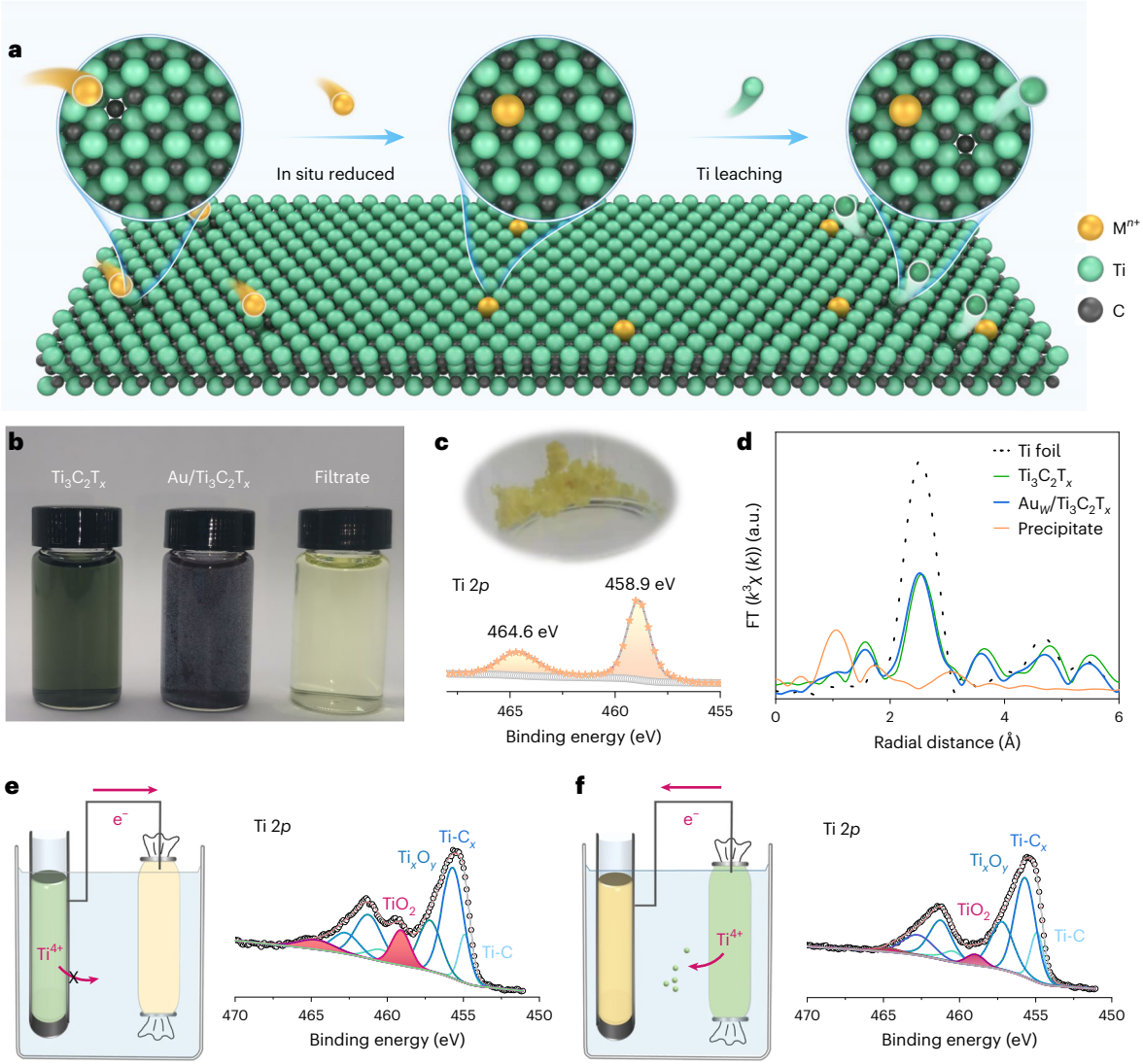

Fig. 2 | Ti leaching during in situ reducing processes. a, A schematic illustration of the Ti metal dissolution process. **b**, A photograph of the solution state during liquid-phase reduction. **c**, The powder obtained by freeze drying a large amount of filtrate and its Ti 2*p* spectrum. **d**, The Fourier transform (FT)–EXAFS curves of $Ti_3C_2T_x$, $Au_W/Ti_3C_2T_x$, precipitate and Ti foil. **e**,**f**, A schematic of Ti metal leaching and Ti 2*p* spectra of $Au/Ti_3C_2T_x$ samples collected in crucibles (**e**) and semipermeable membranes (**f**). The green, yellow and blue solutions represent $Ti_3C_2T_x$, $HAuCl_4$ and NaCl aqueous solutions, respectively.

the charge distribution on the surface of the $Ti_3C_2T_x$ MXene. While the $Ti_3C_2T_x$ MXene surface is negatively charged, its edges exhibit a positive charge[47,48]. It is well known that the stabilized form of Au^{3+} in aqueous solution is $AuCl_4^-$. Consequently, the attractive forces between the positively charged edge of $Ti_3C_2T_x$ and the negatively charged $AuCl_4^-$ lead to a distinct spatial distribution pattern of Au nanoparticles. To verify this, the $Ti_3C_2T_x$ used for in situ reduction deposition was pre-treated with sodium metasilicate[48], which selectively binds to the edges of the $Ti_3C_2T_x$ nanosheets. Au was then deposited on the surface $Ti_3C_2T_x$ under the same conditions. Transmission electron microscopy (TEM) images show that the reduction reaction can still take place, but the Au nanoparticles are no longer deposited at the edges of the $Ti_3C_2T_x$ nanosheets (Supplementary Fig. 40). This confirms the distinct physicochemical properties between the edges and the surface of $Ti_3C_2T_x$ nanostructures[47].

In addition, the coordination environment of M^{n+} species also plays an important role in determining its deposition location. To validate this, an Au^{3+} ion solution containing EDTA complexing agent was injected into a $Ti_3C_2T_x$ aqueous dispersion at room temperature. The TEM images shown in Fig. 3g and Supplementary Fig. 41 show that Au nanoparticles are uniformly deposited on the surface of the $Ti_3C_2T_x$ MXene, with a lattice spacing of 0.239 nm, which is attributed to the (111) face of the Au nanoparticles[26,49] that have a size of 5 ± 3 nm (Fig. 3h). This indicates that the variation in coordination environment of Au species ($AuCl_4^-$ and Au–EDTA) leads to the selectivity of deposition site. Consequently, this provides an approach for the precise control of metal deposition locations using in situ reduction strategies.

Size distribution of Pd

When Pd^{2+} reacts with $Ti_3C_2T_x$ nanosheets at room temperature, small nanoparticles with characteristics different from Ag and Au are obtained. TEM images of $Pd/Ti_3C_2T_x$ show a uniform size and linear continuous distribution of Pd nanoparticles on the support surface, with an average size of 1–3 nm regardless of the Pd loading (Fig. 4a–d). HAADF–STEM images show the presence of small amounts of Pd atoms around the worm-like Pd nanoparticles (Fig. 4e,f). Interestingly, even at an ultrahigh loading of 50 wt%, the size and morphology of individual Pd nanoparticles remain similar to those observed at a low loading of 2 wt% (Fig. 4g). This accomplishment is challenging to achieve using conventional preparation methods of heterogeneous catalysts. These observations suggest that the migration and agglomeration of Pd on the MXene surfaces are hindered. In addition, the lattice spacing of

https://doi.org/10.1038/s44160-024-00660-z

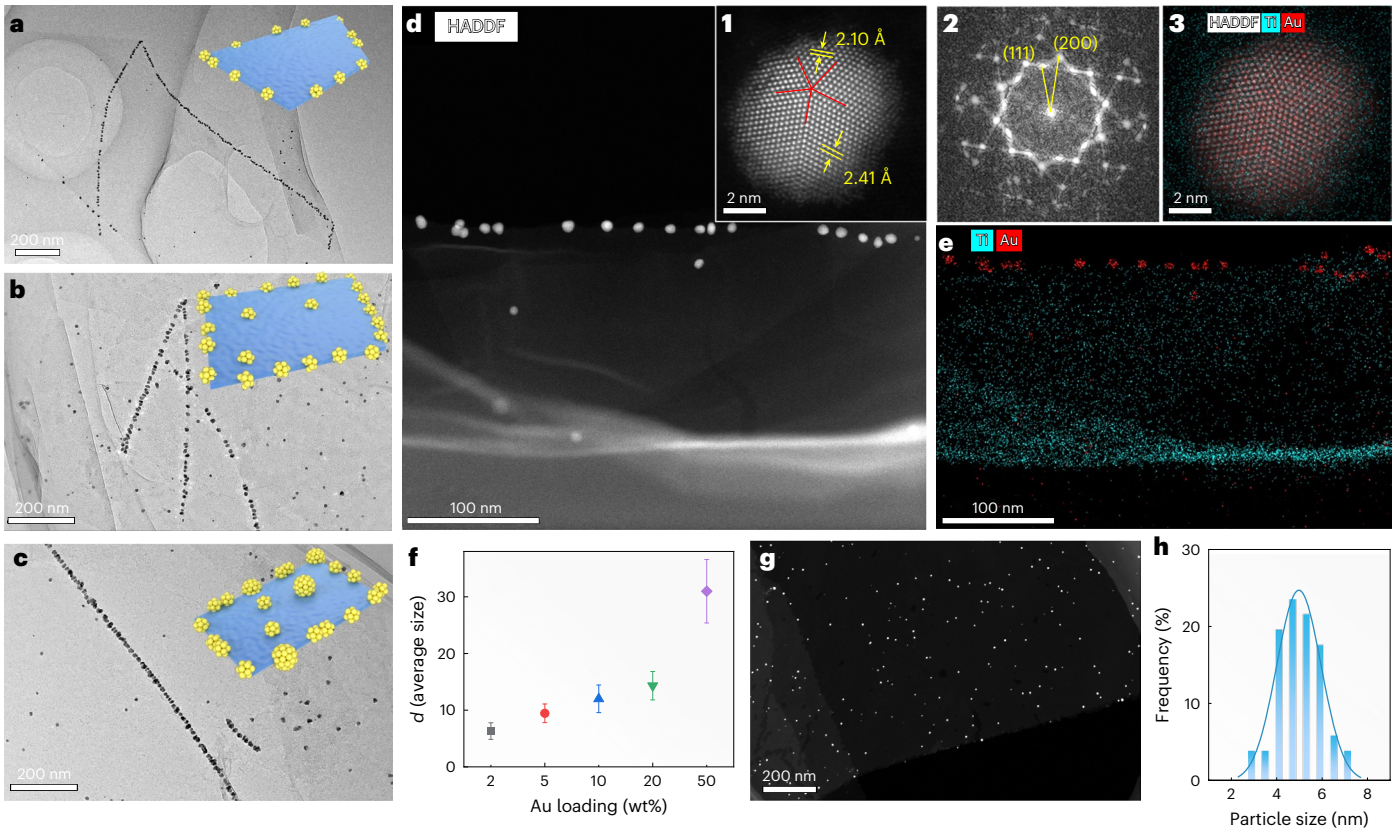

Fig. 3 | Selectivity of the deposition site of Au. a–**c**, TEM images of Au/$Ti_3C_2T_x$ with Au loadings of 2 wt% (**a**), 5 wt% (**b**) and 10 wt% (**c**). The distribution of Au nanoparticles at the edge of $Ti_3C_2T_x$ nanosheets was found in all samples. **d**,**e**, HAADF–STEM images (**d**) and corresponding element maps (**e**) of Au/$Ti_3C_2T_x$-2, and 1, 2 and 3 demonstrate the atomic distribution, pattern diffraction and EDS mapping of Au nanoparticle, respectively. **f**, *d*-related plots as a function of Au loading content. *d* represents Au nanoparticle size and the error bars indicate s.d. based on the statistics of 60–123 Au nanoparticles. **g**,**h**, HAADF–TEM image (**g**) and size distribution (**h**) of Au nanoparticles in Au/$Ti_3C_2T_x$ nanostructures prepared using a complexation strategy. The blue and yellow colours represent the $Ti_3C_2T_x$ nanosheet and Au nanostructures in **a**–**c**, respectively.

the Pd nanoparticles is 0.227 nm (Fig. 4f), slightly larger than that of the conventional Pd (111) crystalline surface[10]. This discrepancy can be attributed to the tensile lattice strain exerted on the Pd nanoparticles due to the large lattice spacing of $Ti_3C_2T_x$.

A larger lattice mismatch between Pd nanoparticles and $Ti_3C_2T_x$ ($\Delta r_{MXene\text{-}Pd}/r_{MXene}$ = 8.1%) leads to a greater strain loss, which prevents the agglomeration of Pd nanoparticles. In contrast, the size of Ag and Au nanoparticles is consistently larger than that of Pd nanoparticles at the same loading (Supplementary Fig. 42). This is due to the relatively small lattice mismatches between Ag and $Ti_3C_2T_x$ (4.2%) and between Au and $Ti_3C_2T_x$ (6.1%). These relatively perfect lattice matches facilitate the continuous growth of nanoparticles on the support surface. Therefore, the size of the metal follows the pattern $R_{Ag\ NPs} > R_{Au\ NPs} > R_{Pd\ NPs}$ at the same loading. This mode of deposition is known as the Volmer–Weber mode[50], which applies not only to the growth of thin films but also to the in situ reduction process. Other metals with larger lattice mismatches, such as Pt ($\Delta r_{MXene\text{-}Pt}/r_{MXene}$ = 8.5%) and Rh ($\Delta r_{MXene\text{-}Rh}/r_{MXene}$ = 11.5%), exhibit similar worm-like structures at higher loadings (Supplementary Figs. 43 and 44). These experimental results further support the application of the Volmer–Weber mode in the in situ reduction process. Thus, the structure and morphology of the metal nanoparticles formed by the heterogeneous deposition of M^{n+} on $Ti_3C_2T_x$ depend on the degree of lattice mismatch between the metal nanoparticles and the carrier.

It is worth emphasizing that, during the deposition of noble metals on MXene using the in situ reduction strategy, no substantial change in the size of the nanosheets was observed (Supplementary Figs. 45–48). This finding demonstrates the unique advantage of samples prepared by the in situ reduction strategy for investigating the structure–performance relationship. These samples could serve as valuable model materials for controlled variable experiments.

Summary of the principles of metal deposition

These experimental phenomena open the door to the design and preparation of M/MXene composites with fine-tuned structures using in situ reduction strategies. After synthesizing a library of monometallic-loaded M/MXene materials using the in situ reduction approach, three key principles can be outlined as follows: (1) reducing power: the redox potential determines whether a metal can be reduced, as in situ reduction involves a redox reaction between the carrier and M^{n+}; (2) deposition location: the coordination environment of M^{n+} influences the deposition location of the metal on MXene (specifically $Ti_3C_2T_x$ MXene); (3) metal size: the lattice mismatch between the metal and the MXene material determines the size of the deposited metal. These principles serve as a basis for explaining and predicting the reduction of metal precursors and the subsequent deposition of metal atoms on MXene, and particularly the deposition behaviour of bimetallic and multiple metals on MXene surfaces. By exploiting these principles, it is expected that engineering the nucleation and growth of metals in the ionic state on MXene will produce nanostructures with unconventional morphologies that may find unique applications in catalysis, sensing and biotechnology.

Application of in situ reduction strategies

Modulation of the size, location and structure of metals represents an effective, albeit challenging, strategy for controlling the functionality

https://doi.org/10.1038/s44160-024-00660-z

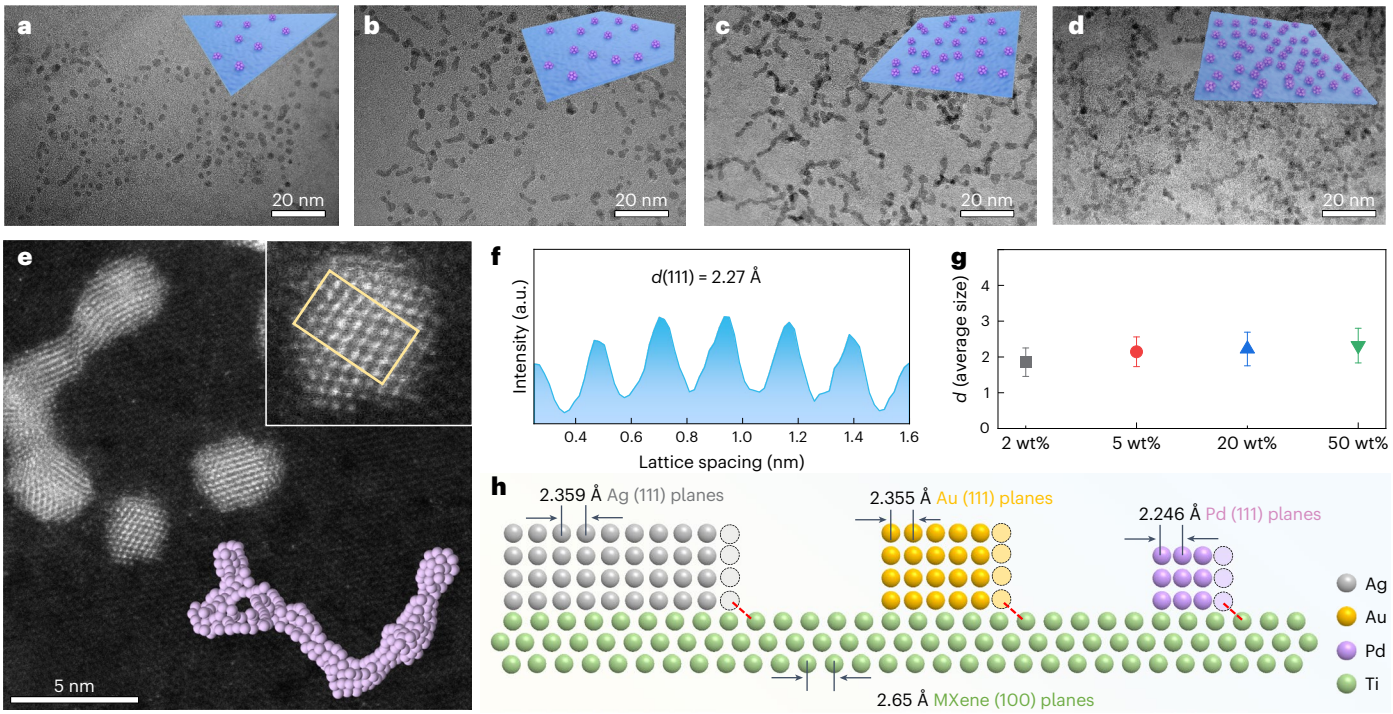

Fig. 4 | Size distribution of Pd. a–**d**, TEM images of Pd/$Ti_3C_2T_x$ with Pd loadings of 2 wt% (**a**), 5 wt% (**b**), 20 wt% (**c**) and 50 wt% (**d**). **e**, A HAADF–STEM image of Pd/$Ti_3C_2T_x$-2 and the inset shows the arrangement of Pd atoms. **f**, The line intensity profile acquired along the yellow square in **e**. **g**, *d*-related plots as a function of Pd loading content. *d* represents Pd nanoparticle size, and the error bars indicate s.d. based on the statistics of 100–150 Pd nanoparticles. **h**, A schematic of metal growth on the MXene surface, here highlighting the lattice mismatch. The blue and purple colours correspond to the $Ti_3C_2T_x$ nanosheet and Pd nanostructures in **a**–**e**, respectively.

of composites[12]. Through in situ reduction strategy, a diverse range of structurally well-defined M/$Ti_3C_2T_x$ composites can be achieved through prediction and design (Fig. 5a). Taking the example of bimetallic Au and Ag, this study demonstrates the synthesis of AgAu alloys and Ag@Au core–shell nanoparticles, and the precise control of their deposition on the surface or edges of MXene materials. Furthermore, the synthesis route for M/MXene is explained through three principles of the in situ reduction strategy.

For the synthesis of $AgAu_{\text{-Edge}}/Ti_3C_2T_x$, aqueous solutions of $HAuCl_4$ and $AgNO_3$ were mixed and added to an aqueous $Ti_3C_2T_x$ solution for reduction. (1) Assessment of reducing ability: $AuCl_4^-$ and Ag^+ possess high redox potentials, and $Ti_3C_2T_x$ has a strong reducing ability towards them; (2) prediction of nucleation sites: $AuCl_4^-$ readily nucleates at the edges of $Ti_3C_2T_x$ nanosheets due to electrostatic adsorption; (3) prediction of metal growth: with a small lattice mismatch between Ag and Au, the remaining $AuCl_4^-$ and Ag^+ grow selectively and rapidly around the Au seeds at the nanosheet edges. As a result, AgAu alloy nanoparticles are deposited at the edges of $Ti_3C_2T_x$ nanosheets. The successful synthesis of $AgAu_{\text{-Edge}}/Ti_3C_2T_x$ composites is confirmed by HAADF–STEM images and STEM–energy-dispersive spectroscopy (EDS) elemental maps (Fig. 5b).

Following the guidance of the three principles of the in situ reduction strategy, the alloy structure of Ag and Au, as well as core–shell structure of Ag@Au, were synthesized on the edge and surface of $Ti_3C_2T_x$ nanosheets, resulting in the formation of $Ag@Au_{\text{-Edge}}/Ti_3C_2T_x$, $AgAu_{\text{-Surface}}/Ti_3C_2T_x$ and $Ag@Au_{\text{-Surface}}/Ti_3C_2T_x$ (Fig. 5c–e and Supplementary Discussion 1). The results presented above clearly demonstrate the effectiveness of the in situ reduction strategy in regulating the size and location of metal deposition on MXene, as well as the ability to tune the structure of metal nanoparticles at the nanoscale. Encouraged by these findings, we have successfully synthesized a series of materials, including $Pd@Au_{\text{-Edge}}/Ti_3C_2T_x$, $Pt@Au_{\text{-Edge}}/Ti_3C_2T_x$, $Au@Ag@Au_{\text{-Surface}}/Ti_3C_2T_x$, $Pt@Ag@Au_{\text{-Surface}}/Ti_3C_2T_x$, $AgPdAu_{\text{-Surface}}/Ti_3C_2T_x$ and $Ag@Pd@Au_{\text{-Edge}}/Ti_3C_2T_x$ (Fig. 5f–k and Supplementary Figs. 49 and 50), by utilizing the $Ti_3C_2T_x$ MXene as a carrier and adjusting the growth conditions for metals. This demonstrates the versatile growth of metals on MXene nanosheets. The control achieved through modulating of the coordination environment of metal ions and the deposition sequence of in situ reduction provides evidence for the feasibility of the in situ reduction strategy, making it a controllable method for manipulating the size, location and structure of metal deposition.

To explore the universality of the in situ reduction method, we have loaded Au, Ag, Pd and various metal combinations onto a variety of MXenes to prepare M/MXene composites, including Mo_2CT_x, V_2CT_x, Ti_3CNT_x, $Nb_4C_3T_x$ and $Mo_2Ti_2C_3T_x$ MXenes (Supplementary Discussion 2 and Supplementary Figs. 51–76). Furthermore, we have examined an array of nanomaterials, including $Ag@Au_{\text{-Edge}}/Ti_3C_2T_x$, for their effectiveness in surface-enhanced Raman spectroscopy as a demonstrative application (Supplementary Discussion 3 and Supplementary Figs. 77–81). These explorations and experimental findings confirm the extensibility and promising applications of the in situ reduction strategy. Although the in situ reduction process may be influenced by more complex factors that warrant further exploration, the results obtained so far are promising. Given the wide range of MXenes available[18,51,52] and the potential combinations with different metals, the in situ reduction strategy opens up numerous possibilities for composite design.

In summary, we have developed a platform for the deposition of metals, including Au, Pd, Ag, Pt, Rh, Ru and Cu, on $Ti_3C_2T_x$ MXene, and a method for the synthesis of M/$Ti_3C_2T_x$ composites with control over their morphology, size and structure. Our results show that $Ti_3C_2T_x$ possesses a general reduction capacity for noble metals and Cu, relying on the redox reaction between M^{n+} and $Ti^{2+/3+}$. The deposition behaviour of the reduced metal is determined by both electrostatic adsorption and lattice spacing. The electrostatic adsorption behaviour determines the metal deposition location, while the lattice spacing governs the size of the deposited metal. These insights into metal–MXene interactions

https://doi.org/10.1038/s44160-024-00660-z

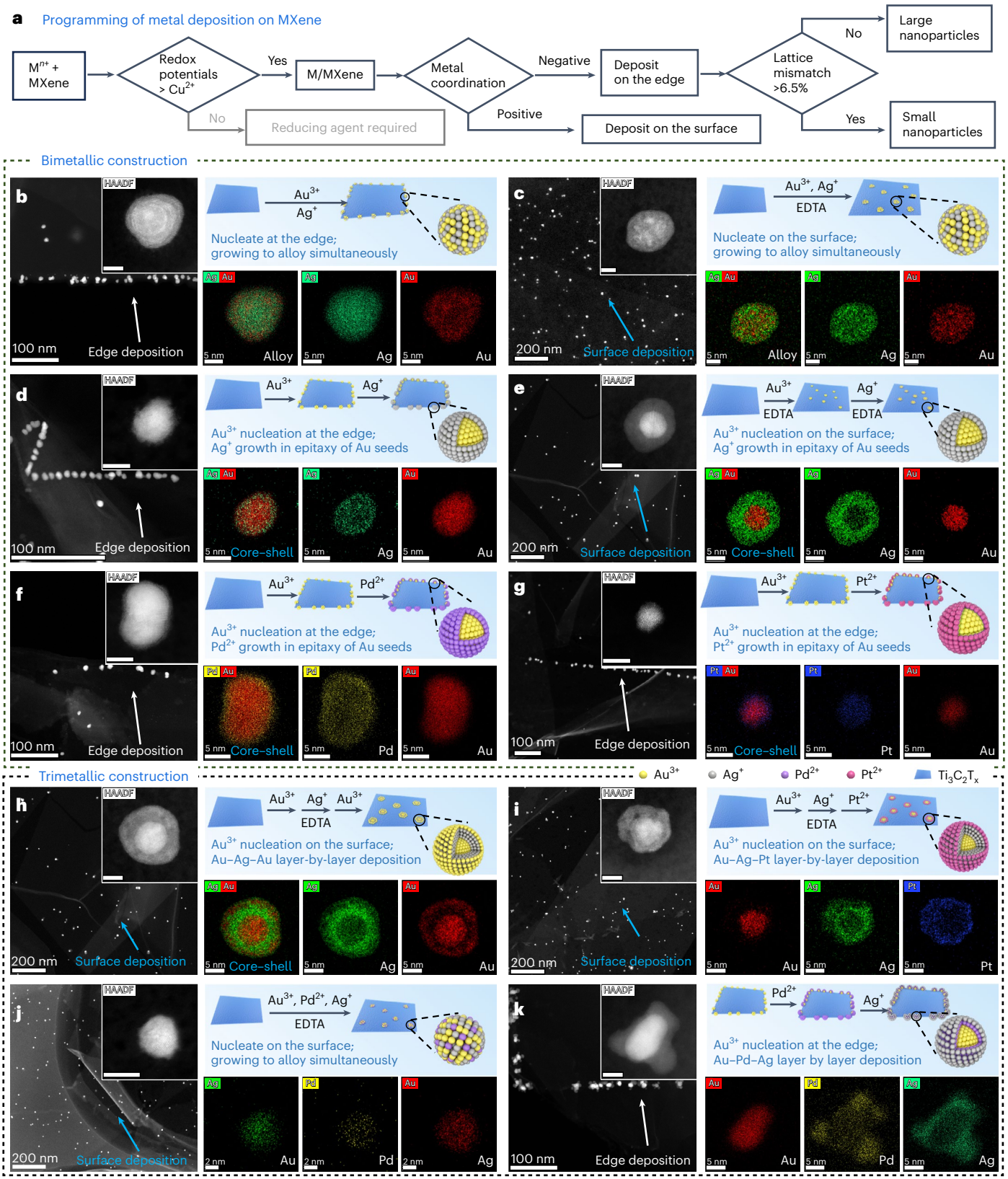

Fig. 5 | Summary of in situ reducing deposition processes. a, Prediction of in situ reduction paths of metal ions on MXene nanosheets. **b**–**k**, Synthesis scheme (top right), HAADF–STEM images (left) and STEM–EDS (bottom right) elemental maps of $AgAu_{-Edge}/Ti_3C_2T_x$ (**b**), $AgAu_{-Surface}/Ti_3C_2T_x$ (**c**), $Ag@Au_{-Edge}/Ti_3C_2T_x$ (**d**), $Ag@Au_{-Surface}/Ti_3C_2T_x$ (**e**), $Pd@Au_{-Edge}/Ti_3C_2T_x$ (**f**), $Pt@Au_{-Edge}/Ti_3C_2T_x$ (**g**), $Au@Ag@Au_{-Surface}/Ti_3C_2T_x$ (**h**), $Pt@Ag@Au_{-Surface}/Ti_3C_2T_x$ (**i**), $AgPdAu_{-Surface}/Ti_3C_2T_x$ (**j**) and $Ag@Pd@Au_{-Edge}/Ti_3C_2T_x$ (**k**) nanostructures, and the structural scheme of metal nanoparticles. Scale bars, 5 nm, in inserted figures.

are important for understanding the in situ reduction approach in M/MXene systems, enabling the design of M/MXene composites with diverse structures, such as bimetallic alloys, core–shell structures and controlled deposition locations. The design strategies for M/$Ti_3C_2T_x$ composite can also be extended to the use of other MXene materials. As an illustrative example, the Ag@$Au_{\text{-Edge}}$/$Ti_3C_2T_x$ composite, characterized with the edge-loading and core–shell structure features, exhibits remarkable performance in surface-enhanced Raman scattering applications. The in situ reduction strategy therefore provides an effective means of tailoring the morphology and structure of M/MXene composites, presenting opportunities for a wide range of nanostructures. The present work will advance both fundamental research and the practical applications of M/MXene, harnessing the potential of the in situ reduction strategy in creating novel nanostructures.

Methods

Synthesis of M/MXene

Freshly prepared monolayer $Ti_3C_2T_x$ MXene colloidal solution was diluted to 100 mg l^{-1} and labelled as solution A. To prepare M/MXene heterojunction materials containing the metals Au, Ag, Pd, Pt, Ru, Rh and Cu, a salt solution containing a certain amount of metal ions was diluted in 10 ml of deionized water, noted as solution B. The corresponding metal sources were $HAuCl_4$, $AgNO_3$, $Pd(NO_3)_2$, K_2PtCl_4, $RuCl_3$, $Rh(NO_3)_3$, $Cu(NO_3)_2$, $NiCl_2$ and $CoCl_2$. Solution B was slowly (1 ml min^{-1}) added to solution A (10 ml) in drops, followed by stirring for 10 min at room temperature. In the preparation of composites with higher metal loadings, the operation is not altered other than by increasing the amount of metal precursor. Precipitates were collected at 10,619*g* or the low metal loading composites were directly freeze dried to separate the M/MXene heterojunction material from the aqueous solvent phase. The resulting material is named as M/$Ti_3C_2T_x$-*y*, where *y* represents the theoretical loading percentage of the metal and M denotes the specific metal. In addition, it has been named following academic conventions to distinct the deposition locations and metal structures. The slash symbol denotes particles that are deposited and allocated on the MXene. The terms 'Surface' and 'Edge' specify the location of metal nanoparticle deposition on MXene nanosheets. The '@' symbol indicates the formation of a core–shell structure with metallic nanoparticles, where the former metal envelops the latter metal. Moreover, metal elements without spaces signify metal nanoparticle alloys containing these metal elements. For instance, AgPdAu$_{\text{-Surface}}$/$Ti_3C_2T_x$ refers to the AgPdAu alloy nanoparticle located on the surface of $Ti_3C_2T_x$ MXene. Meanwhile, Ag@Pd@$Au_{\text{-Edge}}$/$Ti_3C_2T_x$ represents an Ag-encapsulated Pd-encapsulated Au nanoparticle allocated at the edge of $Ti_3C_2T_x$ MXene.

Determination of Ti leach (galvanic cell reaction)

In a primary cell reactor, a colloidal solution of $Ti_3C_2T_x$ MXene was placed in dialysis membranes (cut-off molecular weight of 5,000) and a graphite crucible to act as the positive electrode. The $HAuCl_4$ solution was placed in another dialysis membranes and a graphite crucible to act as a negative electrode. A conductive pathway is formed with graphite rods, conductive copper wires and sodium chloride solution. The concentration of $Ti_3C_2T_x$ colloidal solution and $HAuCl_4$ solution used in this experiment was 1 mg ml^{-1} and 0.203 mM, respectively, and the volume of both solutions was 25 ml. Two solutions in dialysis membranes and graphite crucible were collected after 24 h of reaction and freeze dried and tested.

Synthesis of $Au_{\text{-Surface}}$/$Ti_3C_2T_x$ nanostructures

For the deposition experiments of Au on the surface of $Ti_3C_2T_x$ MXene, EDTA was used as the complexing agent: 0.3 mM EDTA was added into the 0.01 mM $HAuCl_4$ solution with a total volume of 10 ml and stirred to form a complexed metal solution. This solution was then added dropwise to the colloidal solution of $Ti_3C_2T_x$ MXene (10 ml, 100 mg l^{-1}). The subsequent steps of the procedure followed the same protocol as the previous precious metal deposition experiment.

Synthesis of AgAu$_{\text{-Edge}}$/$Ti_3C_2T_x$ nanostructure

An alloy structure loaded on the edge of $Ti_3C_2T_x$ nanosheets (AgAu$_{\text{-Edge}}$/$Ti_3C_2T_x$). To prepare AgAu$_{\text{-Edge}}$/$Ti_3C_2T_x$, 1 mg $Ti_3C_2T_x$ was diluted in 10 ml of aqueous solvent in a beaker. Subsequently, 10 ml of a solution containing $AgNO_3$ (0.0093 mM) and $HAuCl_4$ (0.0051 mM) was slowly added dropwise to the aforementioned solution. This solution was stirred at room temperature for 2 h.

Synthesis of Ag@$Au_{\text{-Edge}}$/$Ti_3C_2T_x$, Pd@$Au_{\text{-Edge}}$/$Ti_3C_2T_x$, Pt@$Au_{\text{-Edge}}$/$Ti_3C_2T_x$ and Ag@Pd@$Au_{\text{-Edge}}$/$Ti_3C_2T_x$ nanostructures

Core–shell structures loaded on the edge of $Ti_3C_2T_x$ nanosheets (Ag@$Au_{\text{-Edge}}$/$Ti_3C_2T_x$). First, 1 mg $Ti_3C_2T_x$ was diluted in 10 ml of aqueous solvent in a beaker. Then 10 ml $HAuCl_4$ (0.0051 mM) was added in the aforementioned solution. After stirring for 1 h, 10 ml of $AgNO_3$ (0.0093 mM) was slowly added dropwise. This solution was stirred at room temperature for 2 h. During the synthesis of Pd@$Au_{\text{-Edge}}$/$Ti_3C_2T_x$ and Pt@$Au_{\text{-Edge}}$/$Ti_3C_2T_x$ composite materials, equivalent volumes of $Pd(NO_3)_2$ (0.0094 mM) and K_2PtCl_4 (0.0051 mM) solutions were used to replace the $AgNO_3$ solution, respectively. The remaining steps were identical to the preparation procedure of Ag@$Au_{\text{-Edge}}$/$Ti_3C_2T_x$. In the preparation of Ag@Pd@$Au_{\text{-Edge}}$/$Ti_3C_2T_x$, after the synthesis of Pd@$Au_{\text{-Edge}}$/$Ti_3C_2T_x$, an additional 10 ml of $AgNO_3$ solution (0.0093 mM) was slowly added dropwise and stirred for 1 h.

Synthesis of AgAu$_{\text{-Surface}}$/$Ti_3C_2T_x$ and AgPdAu$_{\text{-Surface}}$/$Ti_3C_2T_x$ nanostructures

An alloy structure loaded on the surface of $Ti_3C_2T_x$ nanosheets (AgAu$_{\text{-Surface}}$/$Ti_3C_2T_x$). First, 1 mg $Ti_3C_2T_x$ was dispersed in 10 ml of an aqueous solvent in a beaker. Subsequently, a mixture of $AgNO_3$ (0.0093 mM), $HAuCl_4$ (0.0051 mM) and EDTA (0.3 mM) in 10 ml volume was slowly added dropwise. This resulting mixture was stirred at room temperature for 2 h.

For the preparation of AgPdAu$_{\text{-Surface}}$/$Ti_3C_2T_x$, a 10 ml solution comprising $HAuCl_4$ (0.0051 mM), $Pd(NO_3)_2$ (0.0094 mM), $AgNO_3$ (0.0093 mM) and EDTA (0.3 mM) was slowly added dropwise in the $Ti_3C_2T_x$ solution.

Synthesis of Ag@$Au_{\text{-Surface}}$/$Ti_3C_2T_x$, Au@Ag@$Au_{\text{-Surface}}$/$Ti_3C_2T_x$ and Pt@Ag@$Au_{\text{-Surface}}$/$Ti_3C_2T_x$ nanostructures

Core–shell structures loaded on the surface of $Ti_3C_2T_x$ nanosheets (Ag@$Au_{\text{-Surface}}$/$Ti_3C_2T_x$). First, 1 mg of $Ti_3C_2T_x$ was dispersed in 10 ml of aqueous solvent in a beaker. Subsequently, a 10 ml solution containing $HAuCl_4$ (0.0051 mM) and EDTA (0.3 mM) was slowly added to the $Ti_3C_2T_x$ solution. After stirring the reaction for 1 h, a 10 ml mixture of $AgNO_3$ (0.0093 mM) and EDTA (0.3 mM) was introduced into the solution mentioned above.

The two nanostructures, Au@Ag@$Au_{\text{-Surface}}$/$Ti_3C_2T_x$ and Pt@Ag@$Au_{\text{-Surface}}$/$Ti_3C_2T_x$, can be synthesized by adding a solution of $HAuCl_4$ (0.0051 mM) and K_2PtCl_4 (0.0051 mM) to Ag@$Au_{\text{-Surface}}$/$Ti_3C_2T_x$, respectively.

Computational details

The initial atomic structure of the $Ti_3C_2T_x$ nanomaterial was obtained from a previous study or generated using appropriate software. The atomic positions of the $Ti_3C_2T_x$ nanomaterial were fully relaxed through density functional theory calculations to obtain the most stable structure. The Perdew–Burke–Ernzerhof functional was chosen as the exchange–correlation functional.

The surface of the relaxed $Ti_3C_2T_x$ nanomaterial was considered to determine the adsorption sites for the metal ions. The surface was sampled to identify potential adsorption sites, such as bridge sites, hollow sites and top sites.

The metal ions (Au, Ag, Pd, Rh, Ru, Pt and Cu) were individually adsorbed on the identified surface sites of the $Ti_3C_2T_x$ nanomaterial. The adsorption energy (E_{ads}) for each metal ion was calculated using the formula: $E_{ads} = E_{complex} - (E_{metal} + E_{nanomaterial})$, where $E_{complex}$ is the total energy of the metal–ion–$Ti_3C_2T_x$ complex, E_{metal} is the total energy of the isolated metal ion and $E_{nanomaterial}$ is the total energy of the relaxed $Ti_3C_2T_x$ nanomaterial.

The plane-wave cut-off energy was set to a value of the total energy of 400 eV. The Brillouin zone was sampled using an appropriate *k*-point mesh. The Brillouin zone was sampled using a $3 \times 3 \times 1$ *k*-point mesh. Spin polarization was included in the calculations to account for magnetic effects. The final adsorption energies were reported in the reference of the transition metal bulks as comparisons.

Additional methods

For details describing chemicals reagents, material preparation (including the synthesis of MXenes such as $Ti_3C_2T_x$, Ti_3CNT_x, Mo_2CT_x, V_2CT_x, $Nb_4C_3T_x$ and $Mo_2Ti_2C_3T_x$, the detailed procedures for synthesizing expanded M/MXene composites, surface-enhanced Raman spectroscopy measurements and mechanism exploration, as well as the specifics of the mechanism investigation experiments) and characterizations, please see Supplementary Information.

Data availability

Data supporting the findings of this study are available in the article and its Supplementary Information. Source data are provided with this paper.

References

1. Dai, Y. et al. Broadband plasmon-enhanced four-wave mixing in monolayer MoS_2. *Nano Lett.* **21**, 6321–6327 (2021).
2. Li, Y. et al. Superior plasmonic photodetectors based on Au@MoS_2 core–shell heterostructures. *ACS Nano* **11**, 10321–10329 (2017).
3. Park, C. et al. Confinement of ultrasmall bimetallic nanoparticles in conductive metal–organic frameworks via site-specific nucleation. *Adv. Mater.* **33**, 2101216 (2021).
4. Cho, C. et al. Strain-resilient electrical functionality in thin-film metal electrodes using two-dimensional interlayers. *Nat. Electron.* **4**, 126–133 (2021).
5. Zavala, L. A. et al. Direct evidence of the role of Co or Pt, Co single-atom promoters on the performance of MoS_2 nanoclusters for the hydrogen evolution reaction. *ACS Catal.* **13**, 1221–1229 (2023).
6. Shi, Z., Ge, Y., Yun, Q. & Zhang, H. Two-dimensional nanomaterial-templated composites. *Acc. Chem. Res.* **55**, 3581–3593 (2022).
7. Sun, Y. et al. Interface-mediated noble metal deposition on transition metal dichalcogenide nanostructures. *Nat. Chem.* **12**, 284–293 (2020).
8. Li, Z. et al. Reactive metal–support interactions at moderate temperature in two-dimensional niobium-carbide-supported platinum catalysts. *Nat. Catal.* **1**, 349–355 (2018).
9. Wang, M. et al. Site-specified two-dimensional heterojunction of Pt nanoparticles/metal–organic frameworks for enhanced hydrogen evolution. *J. Am. Chem. Soc.* **143**, 16512–16518 (2021).
10. Wei, Z. et al. Tripodal Pd metallenes mediated by Nb_2C MXenes for boosting alkynes semihydrogenation. *Nat. Commun.* **14**, 661 (2023).
11. Feng, R. et al. Epitaxial ultrathin Pt atomic layers on CrN nanoparticle catalysts. *Adv. Mater.* **36**, 2309251 (2024).
12. Tan, J., Li, S., Liu, B. & Cheng, H.-M. Structure, preparation, and applications of 2D material-based metal-semiconductor heterostructures. *Small Struct.* **2**, 2000093 (2021).
13. Sun, Y. et al. Enhancing hydrogen evolution reaction activity of palladium catalyst by immobilization on MXene nanosheets. *ACS Nano* **18**, 6243–6255 (2024).
14. Li, X. et al. Controllable sulfurization of MXenes to in-plane multi-heterostructures for efficient sulfur redox kinetics. *Adv. Energy Mater.* **14**, 2303389 (2024).
15. Zhao, Y. et al. Engineering strategies and active site identification of MXene-based catalysts for electrochemical conversion reactions. *Chem. Soc. Rev.* **52**, 3215–3264 (2023).
16. Li, X. et al. MXene chemistry, electrochemistry and energy storage applications. *Nat. Rev. Chem.* **6**, 389–404 (2022).
17. Dey, A. et al. Doped MXenes—a new paradigm in 2D systems: synthesis, properties and applications. *Prog. Mater Sci.* **139**, 101166 (2023).
18. VahidMohammadi, A., Rosen, J. & Gogotsi, Y. The world of two-dimensional carbides and nitrides (MXenes). *Science* **372**, 1581 (2021).
19. Lim, K. R. G. et al. Fundamentals of MXene synthesis. *Nat. Syn.* **1**, 601–614 (2022).
20. Sikdar, A. et al. Hierarchically porous 3D freestanding holey-MXene framework via mild oxidation of self-assembled MXene hydrogel for ultrafast pseudocapacitive energy storage. *ACS Nano* **18**, 3707–3719 (2024).
21. Lan, L., Jiang, C., Yao, Y., Ping, J. & Ying, Y. A stretchable and conductive fiber for multifunctional sensing and energy harvesting. *Nano Energy* **84**, 105954 (2021).
22. Xi, X. et al. Preparation of Au/Pt/$Ti_3C_2Cl_2$ nanoflakes with self-reducing method for colorimetric detection of glutathione and intracellular sensing of hydrogen peroxide. *Carbon* **197**, 476–484 (2022).
23. Zhu, J. et al. Ultrahigh stable methanol oxidation enabled by a high hydroxyl concentration on Pt clusters/MXene interfaces. *J. Am. Chem. Soc.* **144**, 15529–15538 (2022).
24. Park, S. et al. Reducing the high hydrogen binding strength of vanadium carbide MXene with atomic Pt confinement for high activity toward HER. *Appl. Catal. B* **304**, 120989 (2022).
25. Zhang, J. et al. Single platinum atoms immobilized on an MXene as an efficient catalyst for the hydrogen evolution reaction. *Nat. Catal.* **1**, 985–992 (2018).
26. Li, Z., Huang, W., Liu, J., Lv, K. & Li, Q. Embedding CdS@Au into ultrathin $Ti_{3-x}C_2T_y$ to build dual schottky barriers for photocatalytic H_2 production. *ACS Catal.* **11**, 8510–8520 (2021).
27. Zhao, D. et al. MXene (Ti_3C_2) vacancy-confined single-atom catalyst for efficient functionalization of CO_2. *J. Am. Chem. Soc.* **141**, 4086–4093 (2019).
28. Peng, W. et al. Spontaneous atomic ruthenium doping in Mo_2CT_x MXene defects enhances electrocatalytic activity for the nitrogen reduction reaction. *Adv. Energy Mater.* **10**, e2001364 (2020).
29. Satheeshkumar, E. et al. One-step solution processing of Ag, Au and Pd@MXene hybrids for SERS. *Sci. Rep.* **6**, 32049 (2016).
30. Pandey, R. P. et al. Ultrahigh-flux and fouling-resistant membrane based on layered silver/MXene($Ti_3C_2T_x$) nanosheets. *J. Mater. Chem. A* **6**, 3522–3533 (2018).
31. Zhou, S. et al. Vacancy-rich MXene-immobilized Ni single atoms as a high-performance electrocatalyst for the hydrazine oxidation reaction. *Adv. Mater.* **34**, e2204388 (2022).
32. Xin, W. et al. Lightweight and flexible MXene/CNF/silver composite membranes with a brick-like structure and high-performance electromagnetic-interference shielding. *RSC Adv.* **9**, 29636–29644 (2019).
33. Ghidiu, M., Lukatskaya, M. R., Zhao, M.-Q., Gogotsi, Y. & Barsoum, M. W. Conductive two-dimensional titanium carbide 'clay' with high volumetric capacitance. *Nature* **516**, 78–81 (2014).
34. Shahzad, F. et al. Electromagnetic interference shielding with 2D transition metal carbides (MXenes). *Science* **353**, 1137–1140 (2016).

35. Liu, Y.-T. et al. Self-assembly of transition metal oxide nanostructures on MXene nanosheets for fast and stable lithium storage. *Adv. Mater.* **30**, 1707334 (2018).
36. Zhang, Q. et al. Synergistic photocatalytic-photothermal contribution enhanced by recovered Ag^+ ions on MXene membrane for organic pollutant removal. *Appl. Catal. B* **320**, 122009 (2023).
37. Wang, Y. et al. Titanium carbide MXenes mediated in situ reduction allows label-free and visualized nanoplasmonic sensing of silver ions. *Anal. Chem.* **92**, 4623–4629 (2020).
38. Natu, V. et al. 2D $Ti_3C_2T_z$ MXene synthesized by water-free etching of Ti_3AlC_2 in polar organic solvents. *Chem* **6**, 616–630 (2020).
39. Song, X. et al. Oligolayered $Ti_3C_2T_x$ MXene towards high performance lithium/sodium storage. *Nano Res.* **13**, 1659–1667 (2020).
40. Shekhirev, M. et al. Ultralarge flakes of $Ti_3C_2T_x$ MXene via soft delamination. *ACS Nano* **16**, 13695–13703 (2022).
41. Bao, H. et al. Isolated copper single sites for high-performance electroreduction of carbon monoxide to multicarbon products. *Nat. Commun.* **12**, 238 (2021).
42. Finzel, J. et al. Limits of detection for EXAFS characterization of heterogeneous single-atom catalysts. *ACS Catal.* **13**, 6462–6473 (2023).
43. Zhang, Q. et al. Synthesis of large-area MXenes with high yields through power-focused delamination utilizing vortex kinetic energy. *Adv. Sci.* **9**, e2202748 (2022).
44. Soomro, R. A., Zhang, P., Fan, B., Wei, Y. & Xu, B. Progression in the oxidation stability of MXenes. *Nanomicro Lett* **15**, 108 (2023).
45. Cao, F. et al. Recent advances in oxidation stable chemistry of 2D MXenes. *Adv. Mater.* **34**, 2107554 (2022).
46. Jiang, B. et al. Surface lattice engineering for fine-tuned spatial configuration of nanocrystals. *Nat. Commun.* **12**, 5661 (2021).
47. Natu, V., Sokol, M., Verger, L. & Barsoum, M. W. Effect of edge charges on stability and aggregation of $Ti_3C_2T_z$ MXene colloidal suspensions. *J. Phys. Chem. C* **122**, 27745–27753 (2018).
48. Natu, V. et al. Edge capping of 2D-MXene sheets with polyanionic salts to mitigate oxidation in aqueous colloidal suspensions. *Angew. Chem. Int. Ed.* **58**, 12655–12660 (2019).
49. Jung, Y. et al. Nitrogen-doped titanium carbide ($Ti_3C_2T_x$) MXene nanosheet stack for long-term stability and efficacy in Au and Ag recovery. *Small* **19**, 2305247 (2023).
50. Lon, A., Porter, J., Choi, H. C., Ribbe, A. E. & Buriak, J. M. Controlled electroless deposition of noble metal nanoparticle films on germanium surfaces. *Nano Lett.* **2**, 1067–1071 (2002).
51. Li, Y. et al. A general Lewis acidic etching route for preparing MXenes with enhanced electrochemical performance in non-aqueous electrolyte. *Nat. Mater.* **19**, 894–899 (2020).
52. Li, T. et al. Fluorine-free synthesis of high-purity $Ti_3C_2T_x$ (T=OH, O) via alkali treatment. *Angew. Chem. Int. Ed.* **57**, 6115–6119 (2018).

Acknowledgements

Q.Z. acknowledges support from Institute of Inorganic Membrane Science and Engineering (Shandong University of Technology) and Natural Science Foundation in Shandong Province (ZR2023QB007 and ZR2022QB147) and the Youth Innovation Team of Colleges and Universities in Shandong Province (2023KJ147). H.L. acknowledges support from the National Natural Science Foundation of China (52371140, 21972093 and 21974027), Shanghai Frontiers Science Centre of Biomimetic Catalysis and the Shanghai Engineering Research Centre of Green Energy Chemical Engineering. J.-a.W. acknowledges support from the Welch Foundation (F-1841) Texas Advanced Computing Centre and the Perlmutter at the National Energy Scientific Research Center. C. Zhang acknowledges support from the Program for Eastern Young Scholars in Shanghai and Shanghai Class IV Peak Disciplinary Development Program.

Author contributions

H.L. conceived and supervised the research. Q.Z., Q.Y., C. Zhang and H.L. wrote and revised the paper. Q.Z., Q.Y., Y.F. and C. Zhang designed the experiments. Q.Z., Q.L. and S.X. performed most of the experiments and data analysis. Q.Z., Q.Y., C. Zhang and H.L. discussed and proposed the mechanism. J.-a.W. and Q.L. performed the theoretical calculations. Q.Z., J.-a.W., Q.Y., Q.L., R.F., C.L., Y.F., C. Zhao, W.C., P.J., J.S., C. Zhang, S.X., G.H. and H.L. participated in experiments and discusions. All authors discussed the results and commented on the paper.

Competing interests

The authors declare no competing interests.

Additional information

Supplementary information The online version contains supplementary material available at https://doi.org/10.1038/s44160-024-00660-z.

Correspondence and requests for materials should be addressed to Hui Li.

Peer review information *Nature Synthesis* thanks Khaled A. Mahmoud and the other, anonymous, reviewer(s) for their contribution to the peer review of this work. Primary Handling Editor: Alexandra Groves, in collaboration with the *Nature Synthesis* team.